THE FORWARD–BACKWARD METHOD WITH A NOVEL SPECTRAL ACCELERATION ALGORITHM (FB/NSA) FOR THE COMPUTATION OF SCATTERING FROM TWO-DIMENSIONAL LARGE-SCALE IMPEDANCE RANDOM ROUGH SURFACES

D. Torrungrueng[1] and Joel T. Johnson[1]
[1] ElectroScience Laboratory
Department of Electrical Engineering
The Ohio State University
Columbus, Ohio 43212

Received 22 November 2000

ABSTRACT: *The forward–backward method with a novel spectral acceleration algorithm (FB / NSA) has been shown to be a very efficient $\mathcal{O}(N_{tot})$ iterative method of moments, where N_{tot} is the total number of unknowns to be solved, for the computation of electromagnetic wave scattering from two-dimensional (2-D) perfectly conducting rough surfaces. In this paper, the method is extended to treat impedance rough surfaces. It is found that the 2-D NSA algorithm for the impedance case is similar to the one for the perfectly conducting case. Comparisons of numerical results between the standard 2-D FB and 2-D FB / NSA methods show that the latter yields very accurate results with an appreciable reduction of CPU time.* © 2001 John Wiley & Sons, Inc.
Microwave Opt Technol Lett 29: 232–236, 2001.

Key words: *forward–backward method; novel spectral acceleration algorithm; rough surface scattering*

1. INTRODUCTION

Recently, the forward–backward method with a novel spectral acceleration algorithm (FB/NSA) has been shown to be a very efficient $\mathcal{O}(N_{\text{tot}})$ iterative method of moments for the computation of electromagnetic (EM) wave scattering from two-dimensional (2-D) perfect electric conducting (PEC) rough surfaces (3-D scattering problems), where N_{tot} is the total number of unknowns to be solved [1]. In this paper, the 2-D FB/NSA algorithm for 2-D *impedance* rough surfaces is formulated using the impedance boundary condition (IBC) approximation [2]. The new algorithm is thus an extension of the 2-D FB/NSA algorithm developed for 2-D PEC rough surfaces [1] to take the *finite* conductivity of the medium below the surface profile into account. It is found that two additional terms are required in the MFIE for the PEC case to account for *nonzero* surface impedance, and one of them involves the surface divergence of the associated currents which requires a numerical differentiation. Unlike the PEC case, each current element on the surface is always coupled to another, even for a *linear* surface model. However, a 2-D NSA algorithm for the IBC case can still be formulated which is similar to the PEC case. For large-scale IBC rough surfaces, comparisons of numerical results between the conventional FB method and the 2-D FB/NSA method illustrate that the latter yields identical results to the former, with an appreciable reduction of CPU time.

This paper is organized as follows. The FB method for 2-D IBC rough surfaces is described in Section 2. Section 3 presents the formulation of the 2-D NSA algorithm for IBC rough surfaces. To illustrate the accuracy and efficiency of the 2-D FB/NSA algorithm for IBC rough surfaces, numerical results are illustrated in Section 4, and Section 5 presents conclusions.

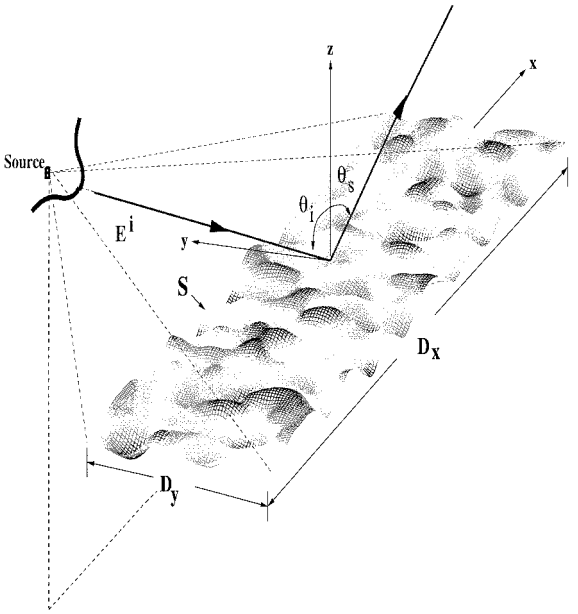

Figure 1 A 2-D PEC rough surface profile S illuminated by a *tapered* incident field $\mathbf{E}^i(x, y, z)$ centered at the origin and propagating in direction $\hat{k}_i = \hat{x}\sin\theta_i\cos\phi_i + \hat{y}\sin\theta_i\sin\phi_i - \hat{z}\cos\theta_i$

2. THE FB METHOD FOR IMPEDANCE ROUGH SURFACES

Consider a 2-D rough surface profile S illuminated by an incident field $\mathbf{E}^i(x, y, z)$ centered in direction $\hat{k}_i = \hat{x}\sin\theta_i\cos\phi_i + \hat{y}\sin\theta_i\sin\phi_i - \hat{z}\cos\theta_i$, as shown in Figure 1, where θ_i and ϕ_i refer to the incident polar and azimuthal angles, respectively. The region above the surface profile is assumed to be free space, and the region below is assumed to be a homogeneous, *nonmagnetic*, and isotropic medium described by electric permittivity ϵ_1 and magnetic permeability μ_0. The surface height function $z = f(x, y)$ has zero mean, and its maximum and minimum height variations are denoted by $z_{\max}$ and $z_{\min}$, respectively. Let $\Delta z_{\max}$ denote the largest surface variation, which is equal to $z_{\max} - z_{\min}$, and let $\mathbf{r} = \hat{x}x + \hat{y}y + \hat{z}z$ and $\mathbf{r}' = \hat{x}x' + \hat{y}y' + \hat{z}z'$ denote a field point and a source point on the rough surface, respectively. The incident field $\mathbf{E}^i(x, y, z)$ is tapered with a Gaussian beam amplitude pattern confining the illuminated rough surface to the rectangular surface area $D_x \times D_y$ so that surface edges do not contribute strongly to obtained scattered fields. The tapered incident field is discussed in detail in [3–5].

Consider the Stratton–Chu integral equation for the magnetic field in the upper region above the surface profile [6]:

$$\frac{\mathbf{n}\times\mathbf{H}(\mathbf{r})}{2} = \mathbf{n}\times\mathbf{H}^i + \mathbf{n}\times\iint_{PV,\,S_{xy}} dx'\,dy' \times\Big\{-i\omega\epsilon g(\mathbf{r},\mathbf{r}')[\mathbf{n}'\times\mathbf{E}(\mathbf{r}')] + \nabla g(\mathbf{r},\mathbf{r}') \times[\mathbf{n}'\times\mathbf{H}(\mathbf{r}')] - \frac{i|\mathbf{n}'|}{\omega\mu_0}\nabla g(\mathbf{r},\mathbf{r}')\nabla_s' \cdot[\hat{n}'\times\mathbf{E}(\mathbf{r}')]\Big\} \quad (1)$$

where the above integral is a principal-value integral, $\nabla_s' \cdot$ is the surface divergence operator, the 3-D free space Green's function $g(\mathbf{r}, \mathbf{r}') = e^{ikR}/4\pi R$, $\mathbf{n} = \hat{z} - \hat{x}(\partial f/\partial x) - \hat{y}(\partial f/\partial y)$, $\mathbf{n}' = \hat{z} - \hat{x}(\partial f/\partial x') - \hat{y}(\partial f/\partial y')$, $R = |\mathbf{r} - \mathbf{r}'|$, and $\mathbf{H}^i$ is the incident magnetic field associated with $\mathbf{E}^i$. The normal vectors $\mathbf{n}$ and $\mathbf{n}'$ (*not* unit vectors) point upward from the rough surface S, and S_{xy} is the surface obtained from the projection of the rough surface S onto the xy-plane. For convenience in analysis, define the following quantities: $\mathbf{J}(\mathbf{r}) = \mathbf{n} \times \mathbf{H}(\mathbf{r})$, $\mathbf{J}_{\mathrm{PO}}(\mathbf{r}) = 2\mathbf{n} \times \mathbf{H}^i(\mathbf{r})$, $\mathbf{M}(\mathbf{r}) = \mathbf{E}(\mathbf{r}) \times \mathbf{n}$, and $\mathbf{T}(\mathbf{r}) = \mathbf{M}(\mathbf{r})/|\mathbf{n}|$. Using the impedance boundary condition [2],

$$\hat{n} \times \mathbf{E} = \eta_s \hat{n} \times \hat{n} \times \mathbf{H} \tag{2}$$

where $\hat{n}$ is a unit normal vector pointing out of the rough surface into the upper region, and the surface impedance η_s is typically set to be the characteristic impedance of the lower medium (i.e., $\eta_s = \sqrt{\mu_0/\epsilon_1}$); $\mathbf{J}(\mathbf{r})$ and $\mathbf{M}(\mathbf{r})$ are related via the following equation:

$$\mathbf{M}(\mathbf{r}) = -\eta_s \hat{n} \times \mathbf{J}(\mathbf{r}). \tag{3}$$

Using the above definitions, Eq. (1) can be expressed as the magnetic-field integral equation (MFIE) for an impedance surface as follows:

$$\mathbf{J}(\mathbf{r}) = \mathbf{J}_{\mathrm{PO}}(\mathbf{r}) + \mathbf{J}_{\mathrm{PEC}}(\mathbf{r}) + 2\mathbf{n} \times \iint_{PV,\, S_{xy}} dx'\, dy' \times \left\{ i\omega\epsilon g(\mathbf{r}, \mathbf{r}')\mathbf{M}(\mathbf{r}') - \frac{\nabla g(\mathbf{r}, \mathbf{r}')|\mathbf{n}'|}{i\omega\mu_0} \nabla_s' \cdot \mathbf{T}(\mathbf{r}') \right\} \tag{4}$$

$$\mathbf{J}_{\mathrm{PEC}}(\mathbf{r}) = 2\mathbf{n} \times \iint_{PV,\, S_{xy}} dx'\, dy' \nabla g(\mathbf{r}, \mathbf{r}') \times \mathbf{J}(\mathbf{r}'). \tag{5}$$

Note that Eq. (4) is reduced to the MFIE for the PEC case when $\eta_s = 0$, and two additional terms are required to account for nonzero surface impedance. Using pulse basis functions and delta testing functions (i.e., point matching), the above MFIE can be discretized into the following MM matrix equation [7]:

$$\overline{\overline{Z}}\,\overline{I} = \overline{V} \tag{6}$$

where $\overline{\overline{Z}}$ is the $N_{\mathrm{tot}} \times N_{\mathrm{tot}}$ MM impedance matrix, $\overline{V}$ is the $N_{\mathrm{tot}} \times 1$ excitation vector, $\overline{I}$ is the $N_{\mathrm{tot}} \times 1$ solution vector, $N_{\mathrm{tot}} = 2NM$ is the total number of unknowns on the surface S, and N and M are the numbers of grid cells of S_{xy} along the x- and y-directions, respectively. Using a *linear* surface model (no surface curvature), it can be shown that the principal-value integrals involving $\nabla g(\mathbf{r}, \mathbf{r}')$ are zero when the testing and integration points overlap (self-term calculation) for surfaces approximated by collections of planes. However, the 3-D scalar free-space Green's function $g(\mathbf{r}, \mathbf{r}')$ has singularity contributions when the testing and integration points overlap which can be analytically integrated [5].

Note also that the surface divergence term in Eq. (4) requires a numerical differentiation, a centered difference derivative, of the unknown function $\mathbf{T}(\mathbf{r}')$ as follows:

$$\nabla_s' \cdot \mathbf{T}(\mathbf{r}') \approx \frac{\partial T_x}{\partial x'} + \frac{\partial T_y}{\partial y'} \approx \frac{T_x^{(n+1,m)} - T_x^{(n-1,m)}}{2\Delta x} + \frac{T_y^{(n,m+1)} - T_y^{(n,m-1)}}{2\Delta y} \tag{8}$$

where $n = 1, \ldots, N$ and $m = 1, \ldots, M$. Derivatives at points on surface edges are computed by assuming that currents at the adjacent point are zero; note that this is not a large source of error since a tapered incident field will be used to eliminate fields at surface edges.

Following the FB procedure as given in [1], two FB coupled integral equations for the IBC case at the kth ($k \geq 1$) iteration are obtained:

$$\begin{aligned}\mathbf{J}^{f,(k)}(\mathbf{r}) &= \mathbf{J}_{\mathrm{PO}}(\mathbf{r}) + 2\mathbf{n} \times \iint_{PV,\, S_{xy}^f} dx'\, dy' \nabla g(\mathbf{r}, \mathbf{r}') \times [\mathbf{J}^{f,(k)}(\mathbf{r}') + \mathbf{J}^{b,(k-1)}(\mathbf{r}')] + 2\mathbf{n} \times \iint_{PV,\, S_{xy}^f} dx'\, dy' \\ &\quad \times \left\{ -i\omega\epsilon\eta_s g(\mathbf{r}, \mathbf{r}')\hat{n}' \times [\mathbf{J}^{f,(k)}(\mathbf{r}') + \mathbf{J}^{b,(k-1)}(\mathbf{r}')] + \frac{\nabla g(\mathbf{r}, \mathbf{r}')|\mathbf{n}'|\eta_s}{i\omega\mu_0} \nabla_s' \cdot \left[\frac{\hat{n}' \times (\mathbf{J}^{f,(k-\frac{1}{2})}(\mathbf{r}') + \mathbf{J}^{b,(k-1)}(\mathbf{r}'))}{|\mathbf{n}'|} \right] \right\}\end{aligned} \tag{9}$$

$$\begin{aligned}\mathbf{J}^{b,(k)}(\mathbf{r}) &= 2\mathbf{n} \times \iint_{PV,\, S_{xy}^b} dx'\, dy' \nabla g(\mathbf{r}, \mathbf{r}') \times [\mathbf{J}^{f,(k)}(\mathbf{r}') + \mathbf{J}^{b,(k)}(\mathbf{r}')] + 2\mathbf{n} \times \iint_{PV,\, S_{xy}^b} dx'\, dy' \\ &\quad \times \left\{ -i\omega\epsilon\eta_s g(\mathbf{r}, \mathbf{r}')\hat{n}' \times [\mathbf{J}^{f,(k)}(\mathbf{r}') + \mathbf{J}^{b,(k)}(\mathbf{r}')] + \frac{\nabla g(\mathbf{r}, \mathbf{r}')|\mathbf{n}'|\eta_s}{i\omega\mu_0} \nabla_s' \cdot \left[\frac{\hat{n}' \times (\mathbf{J}^{f,(k-\frac{1}{2})}(\mathbf{r}') + \mathbf{J}^{b,(k)}(\mathbf{r}'))}{|\mathbf{n}'|} \right] \right\}\end{aligned} \tag{10}$$

with the following initialization:

$$\mathbf{J}^{b,(0)}(\mathbf{r}) = \mathbf{0} \tag{11}$$

where $\mathbf{J}^{f,(k)}(\mathbf{r})$ and $\mathbf{J}^{b,(k)}(\mathbf{r})$ are the forward-stepping (FS) and backward-stepping (BS) currents, respectively, and the surfaces S_{xy}^f and S_{xy}^b correspond to the FS and BS processes, respectively (see [1, Fig. 3(d)]). In Eqs. (9) and (10), the surface divergence term associated with $\mathbf{J}^{f,(k-(1/2))}(\mathbf{r}')$ can be approximately computed via a centered difference derivative [see Eq. (8)] as

$$\nabla_s' \cdot \mathbf{U}^{(k-\frac{1}{2})}(\mathbf{r}') \approx \frac{U_x^{(k-1),(n+1,m)} - U_x^{(k),(n-1,m)}}{2\Delta x} + \frac{U_y^{(k-1),(n,m+1)} - U_y^{(k),(n,m-1)}}{2\Delta y} \tag{12}$$

where the vector $\mathbf{U}^{(k-\frac{1}{2})}(\mathbf{r}')$ is defined as

$$\mathbf{U}^{(k-\frac{1}{2})}(\mathbf{r}') = \frac{\hat{n}' \times \mathbf{J}^{f,(k-\frac{1}{2})}(\mathbf{r}')}{|\mathbf{n}'|}. \tag{13}$$

Note that $U_j^{(k),(n,m)}$ denotes the jth component of $\mathbf{U}(\mathbf{r}')$ at the (n,m)th element on the rough surface S for the kth iteration, and the computation of $\nabla_s' \cdot \mathbf{U}^{(k-\frac{1}{2})}(\mathbf{r}')$ in Eq. (12) involves the FS currents $\mathbf{J}^f(\mathbf{r}')$ at the kth and $(k-1)$th iterations. The reason for using $\mathbf{J}^{f,(k-1)}(\mathbf{r}')$ is that the FS currents $\mathbf{J}^{f,(k)}(\mathbf{r}')$ at the kth iteration have not been computed yet in the FS process for the elements above and on the right of the test point located in the (n,m)th element. In Eq. (9), the currents $\mathbf{J}^{f,(k)}(\mathbf{r})$ are first solved for all receiving elements, and then are employed in Eq. (10) to solve for the currents $\mathbf{J}^{b,(k)}(\mathbf{r})$ for all receiving elements. It should be pointed out that, for each (n,m)th receiving element, it is required to invert a 2×2 submatrix in order to solve for $\mathbf{J}^{f,(k)}(\mathbf{r})$ or $\mathbf{J}^{b,(k)}(\mathbf{r})$ due to the coupling between $J_x(\mathbf{r})$ and $J_y(\mathbf{r})$ in matrix self-terms. The iterative process is continued in the FB fashion until the surface currents exhibit convergence to within a specified accuracy criterion.

The FB method usually provides very rapid convergence in many RSS problems of interest; however, it is an $\mathcal{O}(N_{\text{tot}}^2)$ iterative method due to its direct computation of the matrix–vector multiplies to compute the mutual coupling between all pairs of points on the rough surface. In addition, the impedance matrix $\overline{\overline{Z}}$ must be stored at a cost of $\mathcal{O}(N_{\text{tot}}^2)$ memory storage or all elements of the matrix must be recomputed at each iteration with a time-consuming computation. To accelerate the FB method, the NSA algorithm is employed to achieve $\mathcal{O}(N_{\text{tot}})$ for both CPU time and memory storage requirements.

3. THE 2-D NSA ALGORITHM FOR IMPEDANCE ROUGH SURFACES

For convenience in discussion, the computation of the FS process associated with the computation of the weak region contribution $\mathbf{J}_w^{f,(k)}(\mathbf{r})$ is considered only. Following the same procedure as in the PEC case [1], $\mathbf{J}_w^{f,(k)}(\mathbf{r})$ can be expressed as

$$\begin{aligned}
\mathbf{J}_w^{f,(k)}(\mathbf{r}) &= 2\mathbf{n} \times \iint_{S_{xy,w}^f} dx'\,dy' \nabla g(\mathbf{r},\mathbf{r}') \\
&\quad \times [\mathbf{J}^{f,(k)}(\mathbf{r}') + \mathbf{J}^{b,(k-1)}(\mathbf{r}')] + 2\mathbf{n} \times \iint_{S_{xy,w}^f} dx'\,dy' \\
&\quad \times \left\{ -i\omega\epsilon\eta_s g(\mathbf{r},\mathbf{r}') \hat{n}' \times [\mathbf{J}^{f,(k)}(\mathbf{r}') + \mathbf{J}^{b,(k-1)}(\mathbf{r}')] \right. \\
&\quad + \frac{\nabla g(\mathbf{r},\mathbf{r}')|\mathbf{n}'|\eta_s}{i\omega\mu_0} \nabla_s' \\
&\quad \left. \cdot \left[\frac{\hat{n}' \times (\mathbf{J}^{f,(k-\frac{1}{2})}(\mathbf{r}') + \mathbf{J}^{b,(k-1)}(\mathbf{r}'))}{|\mathbf{n}'|} \right] \right\}
\end{aligned} \tag{14}$$

where $S_{xy,w}^f$ is the weak region in the FS process (see [1, Fig. 4]). The currents $\mathbf{J}_w^{f,(k)}(\mathbf{r})$ are computed using the 2-D NSA algorithm for IBC surfaces.

Using the spectral integral representation of the free-space 3-D scalar Green's function in the x-direction with appropriate contour deformation [1], $\mathbf{J}_w^{f,(k)}(\mathbf{r})$ can be re-expressed in terms of the complex vector *radiation* function $F^{(k)}(\mathbf{r}, k_z, k_y)$ on the kth iteration as follows:

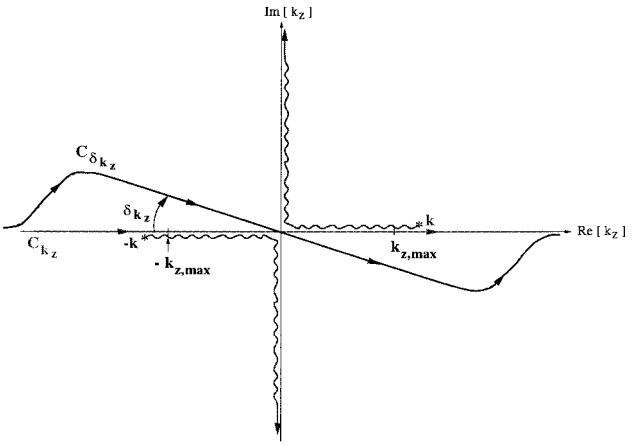

Figure 2 Integration contour of $g(\mathbf{r},\mathbf{r}')$ and $\nabla g(\mathbf{r},\mathbf{r}')$ on the complex k_z-plane. The original contour C_{k_z} is deformed to the new contour $C_{\delta_{k_z}}$

$$\mathbf{J}_w^{f,(k)}(\mathbf{r}) = -\frac{1}{4\pi^2}\mathbf{n} \times \int_{C_{\delta_{k_z}}} \int_{C_{\delta_{k_y}}} dk_z\,dk_y \frac{\mathbf{F}^{(k)}(\mathbf{r}, k_z, k_y)}{k_x} \tag{15}$$

where

$$\mathbf{F}^{(k)}(\mathbf{r}, k_z, k_y) = \iint_{S_{xy,w}^f} dx'\,dy' \mathbf{V}^{(k)}(\mathbf{r}') e^{i\mathbf{k}\cdot\mathbf{R}} \tag{16}$$

$$\begin{aligned}
\mathbf{V}^{(k)}(\mathbf{r}') &= (\mathbf{k} - \omega\epsilon\eta_s\hat{n}') \times [\mathbf{J}^{f,(k)}(\mathbf{r}') + \mathbf{J}^{b,(k-1)}(\mathbf{r}')] \\
&\quad + \frac{|\mathbf{n}'|\eta_s\mathbf{k}}{i\omega\mu_0} \nabla_s' \cdot \left[\frac{\hat{n}' \times (\mathbf{J}^{f,(k-\frac{1}{2})}(\mathbf{r}') + \mathbf{J}^{b,(k-1)}(\mathbf{r}'))}{|\mathbf{n}'|} \right]
\end{aligned} \tag{17}$$

and $C_{\delta_{k_z}}$ and $C_{\delta_{k_y}}$ are the deformed contours in the complex k_z- and k_y-planes as shown in Figures 2 and 3, respectively.

Like the PEC case, the vector function $\mathbf{F}^{(k)}(\mathbf{r}, k_z, k_y)$ can be computed from weak element currents in a *recursive*

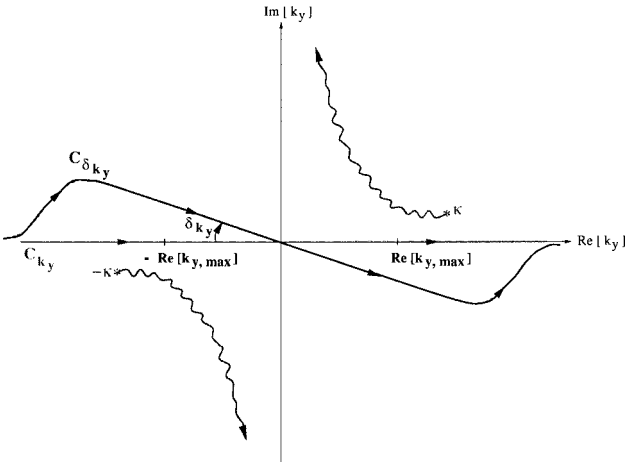

Figure 3 Integration contour of $g(\mathbf{r},\mathbf{r}')$ and $\nabla g(\mathbf{r},\mathbf{r}')$ on the complex k_y-plane for a fixed value of k_z. C_{k_y} is the original contour, and $C_{\delta_{k_y}}$ is the deformed contour

fashion [1]. Equation (15) can be discretized and mapped to the real axis according to the following mappings: $dk_z \rightarrow \Delta k_z e^{-i\delta_{k_z}}$, $k_z \rightarrow k_{z_p} = p\Delta k_z e^{-i\delta_{k_z}}$ for $p = -P, \ldots, P$, $dk_y \rightarrow \Delta k_y e^{-i\delta_{k_y}}$, and $k_y \rightarrow k_{y_q} = q\Delta k_y e^{-i\delta_{k_y}}$ for $q = -Q_p, \ldots, Q_p$, where Δk_z and Δk_y are the integration step sizes in the complex k_z- and k_y-planes, respectively, $P = (k_{z,\max}/\Delta k_z) + 1$, $Q_p = (\mathrm{Re}[k_{y,\max}]/\Delta k_y) + 1$, $k_{z,\max}$ and $\mathrm{Re}[k_{y,\max}]$ are the maximum domains of integration in the complex k_z- and k_y-planes as shown in Figures 2 and 3, respectively, and the total number of plane waves in both planes $Q_{\mathrm{TOT},x}$ is given by

$$Q_{\mathrm{TOT},x} = \sum_{p=-P}^{P} (2Q_p + 1). \tag{18}$$

Finally, the discretized version of Eq. (15) can be written as

$$\begin{aligned}\mathbf{J}_w^{f,(k)}(\mathbf{r}) &= -\frac{1}{4\pi^2}\Delta\Omega \\ &\times \sum_{p=-P}^{P} \sum_{q=-Q_p}^{Q_p} \frac{W(k_{z_p}, k_{y_q})\left[\mathbf{n} \times \mathbf{F}^{(k)}(\mathbf{r}, k_{z_p}, k_{y_q})\right]}{k_{x_{p,q}}} \\ &\times e^{-i\delta_{k_z}} e^{-i\delta_{k_y}}\end{aligned} \tag{19}$$

where $k_{x_{p,q}} = (k^2 - k_{y_q}^2 - k_{z_p}^2)^{\frac{1}{2}}$, $\Delta\Omega = \Delta k_y \Delta k_z$, and $W(k_{z_p}, k_{y_q})$ is a weighting function for numerical integration. The 2-D NSA parameters in both complex k_z- and k_y-planes are

$$\delta_{k_z} = \begin{cases} \dfrac{\pi}{4}, & \tan^{-1}\left(\dfrac{\Delta z_{\max}}{L_x}\right) \le 0.1 \\ \tan^{-1}\beta, & \tan^{-1}\left(\dfrac{\Delta z_{\max}}{L_x}\right) > 0.1 \end{cases} \tag{20}$$

$$k_{z,\max} = \begin{cases} \sqrt{\dfrac{20k}{L_x}}, & \tan^{-1}\left(\dfrac{\Delta z_{\max}}{L_x}\right) \le 0.1 \\ k_{z,s_{\max}} + k_{z,\mathrm{tail}}, & \tan^{-1}\left(\dfrac{\Delta z_{\max}}{L_x}\right) > 0.1 \end{cases} \tag{21}$$

$$\Delta k_z = \frac{1}{22}\sqrt{\frac{C_z k}{L_x}} \tag{22}$$

$$\delta_{k_y} = \gamma \tag{23}$$

$$\mathrm{Re}[k_{y,\max}] = \begin{cases} \sqrt{\dfrac{20k}{L_x}}, & \tan^{-1}\left(\dfrac{D_y}{L_x}\right) \le 0.1 \\ \mathrm{Re}[k_{y,s_{\max}}] + k_{y,\mathrm{tail}}, & \tan^{-1}\left(\dfrac{D_y}{L_x}\right) > 0.1 \end{cases} \tag{24}$$

$$\Delta k_y = \frac{1}{22}\sqrt{\frac{C_y k}{R_{xy}}} \tag{25}$$

where

$$k_{z,s_{\max}} = k\Delta z_{\max}/R_{xz}, \qquad k_{y,s_{\max}} = \kappa D_y/R_{xy},$$

$$R_{xz} = \sqrt{L_x^2 + (\Delta z_{\max})^2}, \qquad R_{xy} = \sqrt{L_x^2 + D_y^2},$$

and $\beta = 1/\max\{\xi, 1\}$, where ξ is the solution of the following nonlinear equation:

$$L_x\sqrt{\tau_1 - \tau_2} + \tau_3 = 0 \tag{26}$$

where $\tau_1 = 0.5\sqrt{4\tau_2^2 + \tau_4^2}$, $\tau_2 = 0.5[k^2(1+\xi)^2 + k_{z,s_{\max}}^2(1-\xi^2)]$, $\tau_3 = (1+\xi)a_{\max} - k_{z,s_{\max}}\Delta z_{\max}$, $\tau_4 = 2\xi k_{z,s_{\max}}^2$, and $a_{\max}$ is some constant (typically found to be less than 3). Note that ξ can be solved numerically via a standard root-finding technique. In addition, there are six unknown constants in the above formulas: γ, $a_{\max}$, $k_{z,\mathrm{tail}}$, $k_{y,\mathrm{tail}}$, C_z, and C_y, and these unknowns can be determined empirically by comparing the analytical solution of $g(\mathbf{r}, \mathbf{r}')$ to the solution obtained from its spectral-domain representation as discussed in detail in [1].

4. NUMERICAL RESULTS

To illustrate the computational efficiency and accuracy of the 2-D FB/NSA algorithm, consider a *deterministic* IBC large-scale rough surface with $\epsilon_{r1} = 10.0 + i10.0$ of size $128\lambda + 16\lambda$ illuminated by a vertical polarized (TM) tapered plane wave with the tapered parameter $g' = 6$ [4] at an incident angle of 40°, where λ is the EM wavelength in free space. The surface of interest is a realization of a Gaussian random process with a Gaussian spectrum given by

$$W(k_x, k_y) = \frac{l_x l_y h^2}{4\pi} e^{-\frac{1}{4}(k_x^2 l_x^2 + k_y^2 l_y^2)} \tag{27}$$

where $W(k_x, k_y)$ represents the spectrum amplitude, l_x and l_y are the correlation lengths in the x- and y-directions, respectively, h is the surface root-mean-square (rms) height, and k_x and k_y are the spatial frequencies in the x- and y-directions, respectively. The surface spectrum parameters of interest are $l_x = l_y = 1.414\lambda$ and $h = 1.0\lambda$. The surface (having $z_{\min} = -3.651\lambda$, $z_{\max} = 4.103\lambda$, and $\Delta z_{\max} = 7.754\lambda$) is sampled with eight points per λ, resulting in 262,144 unknowns for x- and y-polarization surface currents. The following results of CPU time for the above *deterministic* case are based on a Pentium II 333 MHz computer with 128 Mbytes of RAM. The standard 2-D FB method is employed to compare with the 2-D FB/NSA method, and requires six iterations to converge to within 1% accuracy based on the normalized pseudoresidual test [1]. Its total CPU time for this example is 20,990.88 min. The 2-D FB/NSA method employs the following 2-D NSA parameters: $L_x = 4.5\lambda$, $\gamma = 0.08$ rad, $a_{\max} = 2.0$, $k_{z,\mathrm{tail}} = 0.20k$, $k_{y,\mathrm{tail}} = 0.20\,\mathrm{Re}[\kappa]$, $C_z = 10.0$, and $C_y = 15.0$, and requires the same number of iterations to converge within the same accuracy as in the 2-D FB method. However, its total CPU time is only 2368.23 min. Thus, with the 2-D FB/NSA algorithm, a CPU time reduction of 8.86 is achieved in this case.

Numerical results are presented in terms of the normalized bistatic radar cross section (RCS) $\sigma_{\alpha\beta}(\theta_s, \phi_s)$ in the plane of incidence, defined for a scattered wave in α-polarization and an incident wave in β-polarization (see [1, Eq. (34)], where θ_s and ϕ_s refer to the scattered polar and azimuthal angles, respectively. Figure 4(a) and (b) plots the normalized bistatic RCS in decibels versus the scattering angle θ_s when $\phi_i = \phi_s = 0°$ (in plane scattering) for HV and VV polarizations, respectively, comparing between the stan-

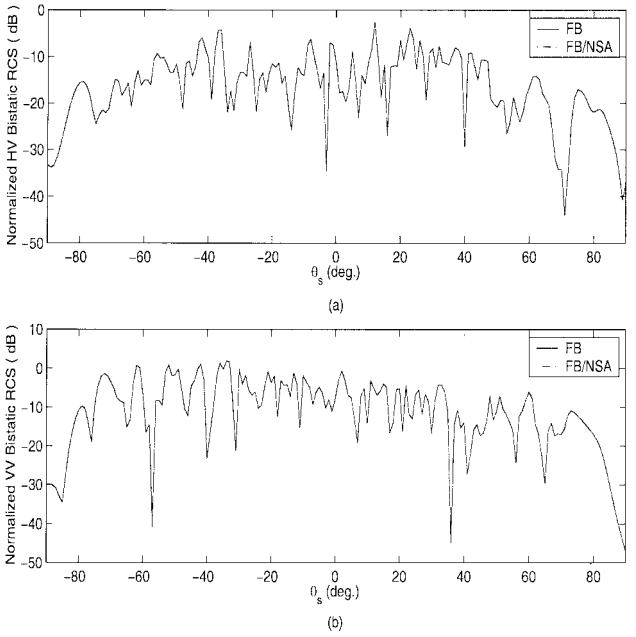

Figure 4 Comparison of the normalized bistatic RCS in decibels by the standard 2-D FB method and the 2-D FB/NSA method for a *deterministic* IBC rough surface with $\epsilon_{r1} = 10.0 + i10.0$ of size $128\lambda \times 16\lambda$ illuminated by a vertical polarized (TM) tapered plane wave with the tapered parameter $g' = 6$ at an incident angle of 40°. The surface of interest is a realization of a Gaussian random process described by a Gaussian spectrum with $l_x = l_y = 1.414\lambda$ and $h = 1.0\lambda$. (a) HV polarization. (b) VV polarization

dard 2-D FB and 2-D FB/NSA methods. From the plots, the normalized bistatic RCSs obtained from both methods are in very good agreement. Thus, the 2-D FB/NSA method provides very accurate results with a great reduction of CPU time.

5. CONCLUSIONS

In this paper, the 2-D FB/NSA algorithm for 2-D PEC surfaces is extended to treat *impedance* rough surfaces. It is found that two additional terms are required in the MFIE formulation for the PEC case to account for *nonzero* surface impedance, and one of them involves the surface divergence of the associated currents which require a numerical differentiation. The 2-D NSA algorithm for the IBC case is similar to the one for the PEC case. Thus, the method is still an $\mathcal{O}(N_{\text{tot}})$ algorithm for a fixed surface dimension in the y-direction D_y, and is most suited for rectangular surfaces due to the treatment of surface cross-range size as a "roughness" parameter. Comparisons of numerical results between the standard 2-D FB and 2-D FB/NSA methods for a deterministic surface have shown that the 2-D FB/NSA method yields very accurate results, with a great reduction of CPU time.

REFERENCES

1. D. Torrungrueng, H.-T. Chou, and J.T. Johnson, A novel acceleration algorithm for the computation of scattering from two-dimensional large-scale perfectly conducting random rough surfaces with the forward-backward method, IEEE Trans Geosci Remote Sensing 38 (2000), 1656–1668.
2. T.B.A. Senior, Impedance boundary conditions for imperfectly conducting surface, Appl Sci Res B 8 (1960), 418–436.
3. D. Torrungrueng, Applications of the novel spectral acceleration (NSA) algorithm for the computation of scattering from rough surfaces, Ph.D. dissertation, The Ohio State University, Columbus, 2000.
4. J.T. Johnson, L. Tsang, R.T. Shin, K. Pak, C.H. Chan, A. Ishimaru, and Y. Kuga, Backscattering enhancement of electromagnetic waves from two-dimensional perfectly conducting random rough surfaces: A comparison of Monte Carlo simulations with experimental data, IEEE Trans Antennas Propagat 44 (1996), 748–756.
5. J.T. Johnson, R.T. Shin, J.A. Kong, L. Tsang, and K. Pak, A numerical study of ocean polarimetric thermal emission, IEEE Trans Geosci Remote Sensing 37 (1999), 8–20.
6. J.A. Kong, Electromagnetic wave theory, Wiley, New York, 1990, 2nd ed.
7. R.F. Harrington, Field computation by moment methods, Krieger, Wiley, Malarbar, FL, 1982.

LOW-LOSS WIDEBAND MICROWAVE COAXIAL BIAS T

V. S. Möttönen,[1] P. Piironen,[1,*] and A. V. Räisänen[1]
[1] Radio Laboratory
Helsinki University of Technology
FIN 02015-HUT, Finland

Received 27 November 2000

ABSTRACT: *A low-loss and well-matched wideband microwave coaxial bias* T *is presented. A simple structure makes the bias* T *easy and low cost to design and fabricate. Test results demonstrate the excellent performance of the bias* T*. The measured return loss is better than 30 dB, and the insertion loss is close to 0.1 dB over a wide frequency range. The 0.5 dB insertion loss bandwidth is 3–16 GHz. Furthermore, the RF isolation is more than 30 dB.* © 2001 John Wiley & Sons, Inc.
Microwave Opt Technol Lett 29: 236–238, 2001.

Key words: *bias* T*; microwave; wideband; coaxial*

1. INTRODUCTION

In many applications, bias Ts are needed to provide an active component with a proper dc operation point while not affecting the RF performance. Although bias Ts often are integrated with the RF circuit, they are also desirable as separate components, especially in test assemblies. Wideband bias Ts have been designed to cover microwave frequencies over a decade bandwidth [1]. However, some applications require lower losses with good matching.

We have designed and constructed a low-loss coaxial bias T for testing of the noise properties of millimeter- and submillimeter-wave planar diodes and mixers where loss and matching characteristics are important. The applied structure enables an easy design and fabrication of a bias T with an excellent performance. The low-loss and low-cost structure makes this bias T competitive with the commercial ones.

2. DESIGN

The design method of the bias T is based on the idea used in constructing microstrip and strip-line bias Ts in [1], extended here to coaxial lines for a low-loss performance. Figure 1

* Present address: European Space Research and Technology Centre, 2200 AG, Noordwijk ZH, The Netherlands.
Contract grant sponsor: European Space Agency/European Space Research and Technology Centre
Contract grant number: ESA/ESTEC Contract 11806/96/NL/CN with DaimlerChrysler Aerospace, Dornier Satellitensysteme GmbH